Fluid Dynamics & Materials Processing

Tech Science Press

http://doi.org/10.32604/fdmp.2026.082466

ARTICLE

CFD Investigation of Solid CO_2 Formation and Dispersion in High-Pressure Pipeline Leakage Events

Hai Yang[1], Chao Yang[1], Guoyong Sui[1], Wendi Yang[1], Zongkai Han[1] and Dan Guo[2,*]

[1]Technology Inspection Center of Shengli Oilfield, SINOPEC, Dongying, China
[2]School of Petroleum Engineering, Shandong Institute of Petroleum and Chemical Technology, Dongying, China
*Corresponding Author: Dan Guo. Email: guodan@sdipct.edu.cn

Received: 16 March 2026; Accepted: 30 June 2026; Published: 31 July 2026

ABSTRACT: This study investigates the leakage and dispersion behavior of high-pressure CO_2 in long-distance pipelines using computational fluid dynamics (CFD) coupled with a regional-scale modeling framework. The influence of key operational and environmental parameters, including transport temperature, pressure, pipeline diameter, leak orifice size, and ambient wind speed, is systematically examined, with particular emphasis on their role in governing the spatial extent of solid CO_2 formation. The results indicate that the evolution of the leakage flow field is governed by a strong coupling between thermodynamic effects and fluid dynamic processes. Elevated temperatures delay the formation of the Mach disk structure, while higher pressures enhance jet momentum, suppress turbulent mixing, and consequently slow the decay of CO_2 concentration. Smaller pipeline and leak diameters promote the development of deep, localized low-temperature cores due to reduced thermal inertia. In contrast, increased wind speeds significantly enhance convective heat and momentum exchange, accelerating both dispersion and warming of the CO_2 plume. Overall, the temperature and pressure state of the transported CO_2 emerges as the primary internal control on dry ice formation, whereas geometric constraints and atmospheric conditions govern the accumulation and transport of cold energy. The findings highlight critical risk conditions associated with low transport temperatures, high operating pressures, small leak diameters, and low-wind environments, which collectively favor the formation of extended solid CO_2 deposition zones.

KEYWORDS: High-pressure CO_2 pipeline; leakage dispersion; solid CO_2 formation; dry ice; computational fluid dynamics

1 Introduction

The Shandong Petrochemical Qilu Petrochemical-Shengli Oilfield CO_2 pipeline is 109 km long, has a design pressure of 12 MPa, and has an annual design transport capacity of 1.7 Mt. It entered operation on 11 July 2023 and is China's first long-distance CO_2 pipeline combining million-ton scale, 100-km-class transport distance, and high-pressure, normal-temperature dense-phase operation [1–3]. This pipeline was selected as a representative test case because its operating pressure, transport capacity, and dense-phase state are typical of long-distance CCUS pipeline systems, while its engineering scale provides realistic boundary conditions for evaluating leakage dispersion and solid CO_2 formation. Pipeline transport is a key component of CCUS because it is safe, economical, and efficient under normal operation [4–8]. However, dense-phase CO_2 pipelines can be damaged by external mechanical interference, wall corrosion, or material defects, leading to leakage, rapid cooling, elevated local CO_2 concentrations, and high-speed jets that may endanger nearby personnel, wildlife, and the environment [9–12]. This study therefore focuses on a vertically upward leakage jet from a local pipeline opening. The scenario is not intended to represent the most common buried-pipeline leakage case. Instead, it represents a high-consequence case that may occur at locally exposed, crossing, station-entry, valve-well, or ground-breakthrough sections where an upward jet can develop. Clarifying the distribution of characteristic parameters after leakage is essential for emergency response and safe operation of long-distance CO_2 pipelines.

Previous studies have examined the consequences of CO_2 pipeline leakage, including industrial-scale release behavior [13–15], leak-diameter effects [16,17], and supercritical initial-stage discharge [18,19]. These studies have mainly focused on CO_2 volume fraction, temperature variation, pressure distribution, and dispersion distance after leakage [20–22]. International work has also advanced discharge and atmospheric-dispersion modeling for high-pressure CO_2 releases, including Phast-based consequence modeling, CFD risk assessment, multiphase RANS jet modeling, CO_2 pipe has source-term and terrain modeling, and COSHER full-bore rupture tests [23–27]. Recent related studies have further examined near-field vertical diffusion of liquid ammonia, far-field dispersion of leaking supercritical CO_2, gas-mixture leakage in confined spaces, and CO_2 condensation theory and applications [28–31]. These studies provide important validation data, modeling strategies, and physical references for release and dispersion hazards. Nevertheless, fewer studies have systematically evaluated the spatial extent of solid CO_2 formation under coupled changes in transport temperature, operating pressure, pipeline diameter, leak diameter, and ambient wind speed.

Most existing studies either simplify the phase-transition process or do not systematically analyze the spatial distribution of dry ice under complex environmental conditions. A key challenge is to couple intense thermodynamic phase change with far-field aerodynamic dispersion without excessive computational cost. To address this problem, this study used a segmented modeling strategy for the multi-stage leakage process, including pipeline depressurization, jet expansion, and far-field convective diffusion. The objective was to clarify high-pressure CO_2 leakage behavior and predict the boundary of dry ice formation for emergency-response planning and safety-distance assessment. In the near-field jet region, a gas-liquid two-phase model was used for Lee-model mass transfer. The possible occurrence of solid CO_2 was then evaluated from the local pressure and temperature relative to the sublimation curve, rather than by extending the Lee model to gas-solid transition. The Peng-Robinson equation of state was used to describe real-gas thermodynamic behavior. The Span-Wagner equation can provide higher accuracy for pure CO_2, but the Peng-Robinson equation was selected to balance computational efficiency and accuracy in three-dimensional multiphase transient simulations. In the far-field diffusion zone, near-field simulation outputs were transferred as source terms and boundary conditions, allowing the thermodynamic effect of dry ice to be retained while improving overall simulation efficiency.

2 Model Establishment

2.1 Basic Assumptions

(1) The leakage process was simulated in two stages. The first stage calculated the source strength of the near-field release, and the resulting source terms were then used as inlet conditions for the second-stage dispersion model.

(2) In the near-field jet model, liquid CO_2 and gaseous CO_2 were treated as the two mass-transfer phases. The Lee model was used only for gas-liquid phase transition. Solid CO_2 was not introduced as an independent Lee-model phase. Instead, the possible dry-ice region was identified from the local thermodynamic state relative to the CO_2 sublimation curve and was coupled through the energy and source-term treatment used to evaluate the dry-ice formation range.

(3) During leakage, the pipeline pressure remained high, so the internal flow was treated as liquid-dominated. The liquid phase was therefore defined as the primary phase, and the gas phase was defined as the secondary phase.
(4) At the initial stage, the thermodynamic state inside the pipeline was assumed to be uniform. A representative leakage section was therefore extracted to reduce computational cost. Considering vortex dissipation near the leakage opening, the length of this pipe section was set to 200 mm to avoid boundary interference.
(5) Phase-change effects were introduced through mass and energy source terms in the mixture model. Heat transfer between the pipe wall and the fluid was not considered.
(6) Terrain effects were ignored, and leakage was assumed to occur over flat ground.

2.2 Basic Governing Equations and Phase Transition Model

(1) Mass conservation equation

$$\frac{\partial \rho}{\partial t} + \nabla \cdot (\rho u) = 0 \tag{1}$$

where ρ is the fluid density, t is time, and u is the velocity vector.

(2) Momentum conservation equation

$$\frac{\partial (\rho u)}{\partial t} + \nabla \cdot (\rho u u) = -\nabla p + \nabla \cdot \left(\tau - \rho u' u'\right) + \rho g + F \tag{2}$$

where p is the static pressure, τ is the viscous stress tensor, ρg is gravity, and F denotes any additional body-force source. No additional momentum source was imposed in this study, so F was set to zero apart from gravity. The Reynolds stress contribution was included through the turbulence closure term in the effective stress divergence.

(3) Energy conservation equation

$$\frac{\partial}{\partial t}\left(\sum_i \alpha_i \rho_i E_i\right) + \nabla \cdot \left(\sum_i \alpha_i u_i (\rho_i E_i + p)\right) = \nabla \cdot \left(k_{eff} \cdot (\nabla T)\right) + S_E \tag{3}$$

where subscript i denotes the i-th phase, α is volume fraction, E is total energy, k_{eff} is effective thermal conductivity, and S_E is the energy source term. S_E includes chemical reaction heat sources, phase change latent heat sources, radiation heat sources, internal excitation heat sources, and mechanical work/viscous dissipation sources. In this paper, the phase change latent heat source of CO_2 is considered.

(4) Turbulence model

SST k-ω model for Jet section

$$\frac{\partial (\rho k)}{\partial t} + \nabla \cdot (\rho u k) = \nabla \cdot \left[\left(\mu + \frac{\mu_{t1}}{\sigma_k}\right) \cdot (\nabla k)\right] + P_k - \beta^* \rho k \omega \tag{4}$$

$$\frac{\partial (\rho \omega)}{\partial t} + \nabla \cdot (\rho u \omega) = \nabla \cdot \left[\left(\mu + \frac{\mu_{t1}}{\sigma_k}\right) \cdot (\nabla \omega)\right] + \alpha \frac{\rho}{\mu_t} P_k - \beta \rho \omega^2 + 2(1 - F_1) \frac{\rho}{\sigma_{\omega^2} \omega} \cdot (\nabla k) \cdot (\nabla \omega) \tag{5}$$

$$\mu_{t1} = \frac{\rho a_1 k}{\max(a_1 \omega, S F_2)} \tag{6}$$

where k is turbulent kinetic energy, ω is specific dissipation rate, μ_{t1} is turbulent viscosity, μ is dynamic viscosity, P_k is the turbulent kinetic-energy generation term, F_1 and F_2 are blending functions, and S is the magnitude of the mean strain-rate tensor in Eq. (6), not an additional turbulence source term. The diffusion and cross-diffusion terms are expressed through the gradients ∇k and $\nabla\omega$, and β^*, β, α, σ_k, σ_ω, and a_1 are empirical model constants.

Standard Realizable k-ε model for the far-field convective diffusion section

$$\frac{\partial(\rho k)}{\partial t} + \nabla\cdot(\rho u k) = \nabla\cdot\left[\left(\mu + \frac{\mu_{t2}}{\sigma_k}\right)\cdot(\nabla k)\right] + P_k - \rho\varepsilon \tag{7}$$

$$\frac{\partial(\rho \varepsilon)}{\partial t} + \nabla\cdot(\rho u \varepsilon) = \nabla\cdot\left[\left(\mu + \frac{\mu_{t2}}{\sigma_k}\right)\cdot(\nabla \varepsilon)\right] + \rho C_1 S\varepsilon - \rho C_2\frac{\varepsilon^2}{k+\sqrt{v\varepsilon}} \tag{8}$$

$$\mu_{t2} = \rho C_\mu \frac{k^2}{\varepsilon} \tag{9}$$

where ε is turbulent dissipation rate, μ_{t2} is turbulent viscosity, C_1 and C_2 are model constants, v is kinematic viscosity, and C_μ is the turbulent-viscosity coefficient.

(5) Component transport model

$$\frac{\partial(\rho Y_i)}{\partial t} + \nabla\cdot(\rho u Y_i) = -\nabla J_i + R_i + S_i \tag{10}$$

where Y is species mass fraction, J is diffusive flux, R is chemical reaction production rate, and S is an additional species source term. In this non-reactive CO_2 leakage problem, R was set to zero. The source term S represented the UDF-based CO_2 mass source transferred from the near-field release calculation to the far-field dispersion model.

(6) Thermodynamic state equation

$$p = \frac{RT}{v-b} - \frac{a\alpha(T)}{v(v+b)+b(v-b)} \tag{11}$$

where p is pressure, T is absolute temperature, v is molar volume, and R is the universal gas constant. In the Peng-Robinson equation of state, $a = 0.45724R^2{T_c}^2/P_c$ and $b = 0.07780RT_c/P_c$.

(7) Phase change model

For pressures above the CO_2 triple-point pressure (p_t = 0.518 MPa), gas-liquid phase transition was described using the Lee model:

$$T > T_{sat}(p) : m_{\mathrm{lg}} = C_{\mathrm{lg}}\alpha_l\rho_l\frac{T - T_{sat}(p)}{T_{sat}(p)} \tag{12}$$

$$T < T_{sat}(p) : m_{\mathrm{lg}} = C_{gl}\alpha_g\rho_g\frac{T_{sat}(p) - T}{T_{sat}(p)} \tag{13}$$

In these equations, subscripts l and g denote the liquid and gas phases, respectively. The evaporation and condensation mass-transfer rates were calculated from the phase volume fractions, densities, and saturation temperature at pressure p. The Lee-model relaxation coefficients were set to 0.1 s^{-1} as a conservative value for gas-liquid mass transfer.

For pressures below the triple-point pressure, the Lee model was not used to describe gas-solid phase transition. Solid CO_2 occurrence was determined only by the thermodynamic criterion:

$$p < p_t, T < T_{sub}(p) \tag{14}$$

where T_{sub} is the sublimation temperature at pressure p. The triple point was therefore used only to select the applicable gas-liquid or gas-solid thermodynamic boundary. It was not used to extend the Lee gas-liquid model to gas-solid or liquid-solid phase transition.

Numerical solution settings. The governing equations were solved using a pressure-based finite-volume CFD solver. Gradients were evaluated using the least-squares cell-based method. Pressure was discretized with the PRESTO! scheme, and momentum, energy, turbulence, and species transport equations were discretized using second-order upwind schemes. Pressure-velocity coupling was handled using the PISO algorithm, and transient terms were advanced with a second-order implicit scheme. The time step was selected based on Courant-number control and monitoring of near-nozzle pressure, temperature, velocity, and CO_2 concentration. The final time-step setting was kept small enough to maintain stable residual convergence and stable monitored flow-field variables. The SST k-ω model was used in the near-field jet region to capture strong adverse pressure gradients and shock-associated shear, whereas the Realizable k-ε model was used in the far-field dispersion region for robust plume-diffusion prediction [32,33].

2.3 Grid Division and Grid Independence Verification

A 300 mm pipe segment was used to represent the local leakage region of the long-distance pipeline. The boundary conditions were defined as follows:

(1) CO_2 inlet: pressure inlet, with CO_2 phase change implemented through the UDF.
(2) Pipe wall: no-slip, adiabatic wall with zero mass flux.
(3) Outlet boundary: pressure outlet, with temperature and pressure matched to ambient conditions.

The computational domain was oriented along the vertically upward leakage-jet direction to represent a high-consequence upward jet from a local pipeline opening, rather than a vertically oriented pipeline layout or the most common buried-pipeline leakage scenario. This scenario may occur at locally exposed sections, suspension-bridge or crossing sections, valve wells, station-entry segments, or cases in which a buried-pipeline rupture breaks through the ground and forms an upward jet. The inlet pipeline region was locally refined, as shown in Fig. 1. Around the leakage port, a linear growth function with a growth factor of 1.05 was used. The computational domain included the internal pipe flow region and the external jet-diffusion region after leakage. The base grid size was 20 mm, and the grid near the leakage port was refined to 1 mm to resolve steep velocity, pressure, and temperature gradients. Standard wall functions were used near solid boundaries, and the dimensionless wall distance y+ was controlled within 30 < y+ < 300. The generated mesh had an average skewness below 0.15 and orthogonal quality above 0.85.

The simulations examined the distributions of temperature, velocity, and CO_2 concentration after pipeline leakage under different transport temperatures (5–45°C), pipeline pressures (8–12 MPa), pipe diameters (100–500 mm), leak apertures (10 mm for a small hole, 40 mm for a large hole, and 300 mm for fracture), and ambient wind speeds (1 and 5 m/s). The dry-ice influence range under these factors was also analyzed. The base case was defined as a transport temperature of 45°C, pipeline pressure of 10 MPa, pipe diameter of 300 mm, leak aperture of 10 mm, and wind speed of 1 m/s.

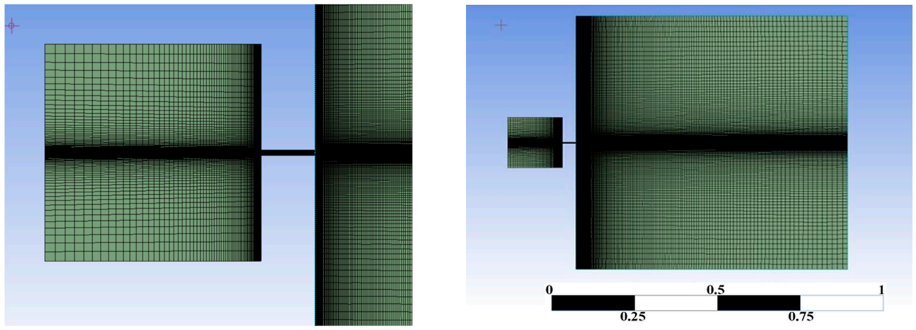

(**a**) Leakage area (**b**) Numerical simulation area

Figure 1: Grid structure division.

To ensure that the numerical results were not controlled by grid resolution, four meshes containing 114,876, 206,628, 304,684, and 401,786 cells were compared. The velocity profiles along the jet axis were used for the grid independence assessment. As shown in Fig. 2, the four velocity curves had highly consistent trends. In the initial stage (0–1 m), velocity increased rapidly, decreased briefly, and then recovered. In the development stage (1–5 m), the growth amplitudes and final convergence values of the four curves were nearly identical, with no obvious separation.

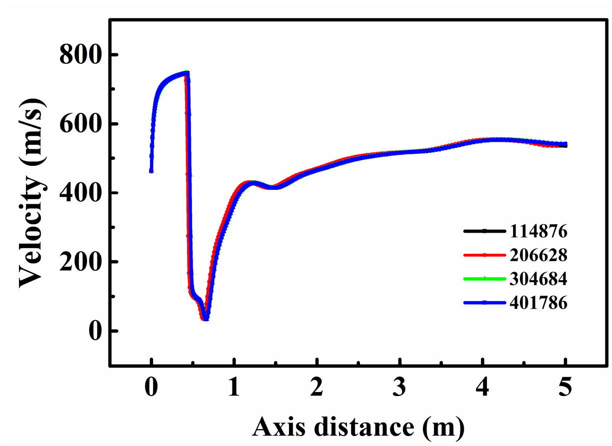

Figure 2: Mesh independence study.

These results indicate that increasing the grid size from 114,876 to 401,786 cells produced only limited changes in the calculated velocity field. The current grid resolution was therefore sufficient for the required accuracy. Further grid refinement would substantially increase computational cost without significantly improving the results. The 114,876-cell mesh was consequently selected for the subsequent simulations to balance computational efficiency and accuracy.

2.4 Model Validation

To verify the reliability of the simulation, the calculated near-field jet structure was compared with the experimental and numerical results reported in Ref. [21], as shown in Fig. 3. The simulation reproduced the Mach disk, which is the characteristic near-field structure of an under-expanded jet, including its disk-like interface and relative distance from the jet outlet. The velocity-field comparison further showed that the model captured the high-speed jet core and the radial attenuation of velocity in the free-expansion region. Downstream of the Mach disk, the simulated contour map also reproduced the reflected shock-wave system and the slip lines along the jet boundary. These flow-field structures were consistent with the shock morphology and slip-line direction shown in the experimental shadowgraph. The modified k-ε result shown in the validation comparison is the benchmark result reported in Ref. [21]. In the present model, the SST k-ω model was used for the near-field jet section, and the standard Realizable k-ε model was used for the far-field convective diffusion section. The Realizable k-ε model was not modified in this study.

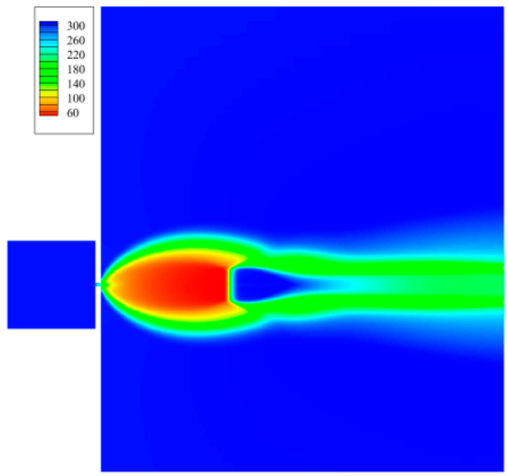

Figure 3: Simulation comparision of under-expanded structures compared with Ref. [21].

3 Results and Analysis

3.1 Distribution of Characteristic Parameters after Leakage

3.1.1 Pipeline Transport Temperature

Fig. 4 shows the cloud diagrams of characteristic parameters after CO_2 leakage under different transport temperatures, and Fig. 5 shows the corresponding axial distributions. The leakage flow field was controlled by coupled isentropic expansion, shock-wave dissipation, and turbulent entrainment, and it depended strongly on the initial temperature. Thermodynamically, expansion from high pressure (8–12 MPa) to the ambient environment (0.1 MPa) caused the 5°C case to cool sharply to below 50 K and to remain below 200 K at an axial distance of 5 m. The 50 K value represents aerodynamic static temperature rather than equilibrium temperature. In the Prandtl-Meyer expansion fan near the nozzle, extremely low pressure and high velocity caused the static temperature of the moving fluid parcel to decrease sharply. Similar sub-100 K static-temperature behavior has been reported in previous CFD studies [21]. In the 45°C case, the temperature remained above 100 K after leakage expansion and recovered to approximately 250 K at an axial distance of 3 m.

Dynamically, higher transport temperature increased sound speed and stagnation enthalpy, delaying the Mach disk from 0.5 m in the 5°C case to 0.8 m in the 45°C case. This reduced shock-wave energy dissipation and changed the post-shock velocity reduction from 450 m/s to below 50 m/s in the low-temperature case to 700 m/s to about 200 m/s in the high-temperature case. These dynamic differences produced distinct CO_2 diffusion morphologies. The 45°C case, with higher momentum flux, enhanced turbulent entrainment and extended the high-concentration CO_2 core beyond 4 m. In contrast, the 5°C case showed rapid concentration decay before 4 m because of weaker momentum and dry-ice deposition.

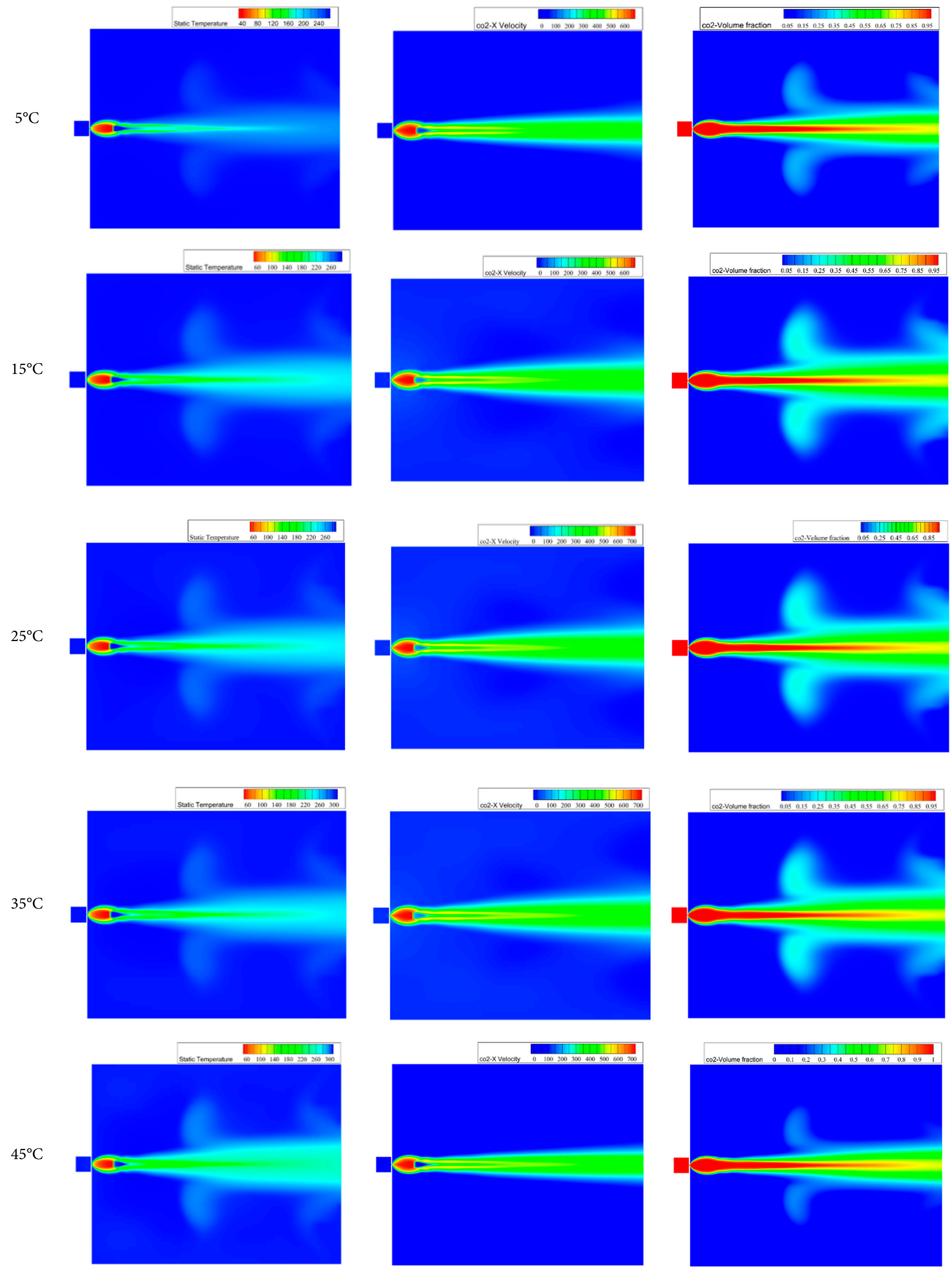

(**a**) Temperature distribution (**b**) Velocity distribution (**c**) Concentration distribution

Figure 4: Cloud diagrams of characteristic parameter distributions after CO_2 leakage under different pipeline transportation temperature conditions.

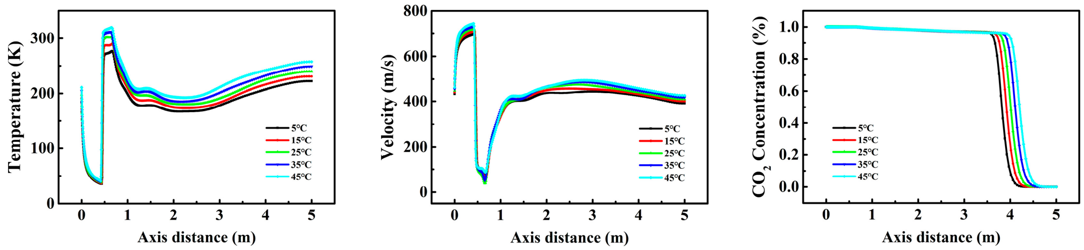

(**a**) Temperature distribution (**b**) Velocity distribution (**c**) Concentration distribution

Figure 5: Distribution curves of axial characteristic parameters after CO_2 leakage under different pipeline transportation temperature conditions.

3.1.2 Pipeline Transport Pressure

Fig. 6 shows the cloud diagrams of characteristic parameters after CO_2 leakage under different transport pressures, and Fig. 7 shows the corresponding axial distributions. The mass transfer of the leakage flow field was governed by the competing effects of pressure-driven momentum flux and turbulent mixing efficiency. In the near-field jet core (0–1 m), CO_2 concentration remained approximately 1.0% under all pressure conditions. After the flow entered the transition zone, the 8 MPa case showed weaker momentum penetration and stronger ambient-air entrainment. As a result, CO_2 concentration decreased to below 0.2% at 1.5 m, and the axial extent of the high-concentration core (>0.85%) was shortest. The sharp concentration boundary was primarily associated with the edge of the under-expanded core and the Mach disk, although numerical diffusion at the grid shear layer may also have contributed. In this simulation, a CO_2 concentration below 1% was taken as an approximate indicator that core diffusion was complete.

In contrast, the 12 MPa case had much higher momentum flux and suppressed turbulent mixing in the shear layer, which delayed concentration attenuation. At a jet distance of 2 m, CO_2 concentration remained above 0.6%, and the high-concentration core remained clearly defined. The drastic parameter variations near the inlet and the apparent reverse or perpendicular propagation in the contour plots are caused by backward decompression waves, transient boiling phase change, and high-speed friction throttling near the leakage port.

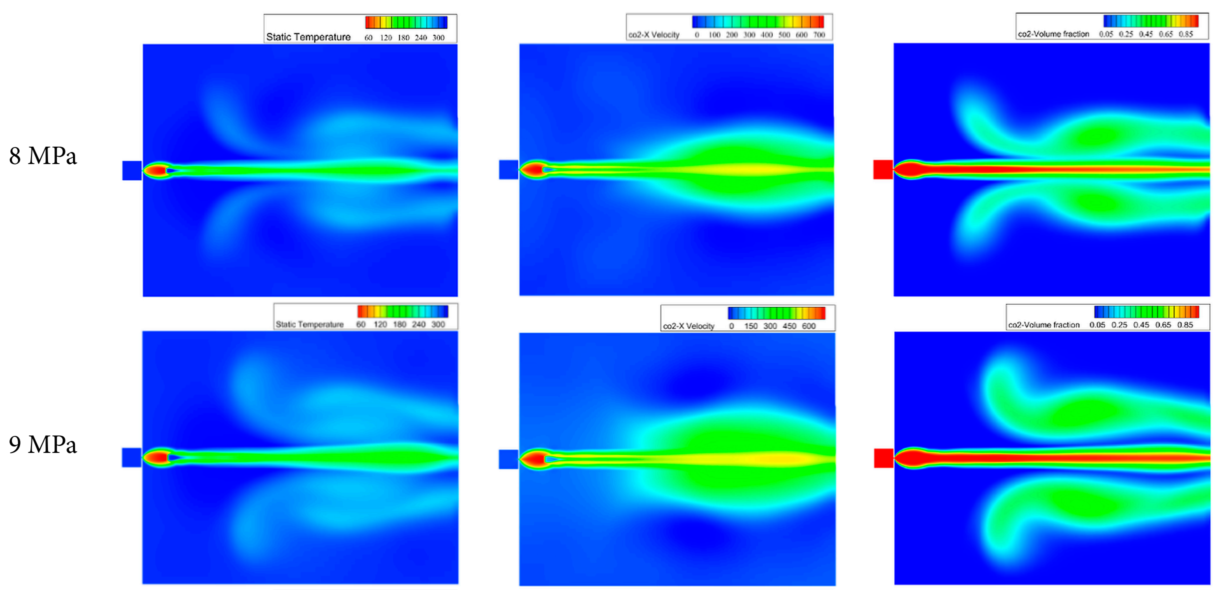

Figure 6: *Cont.*

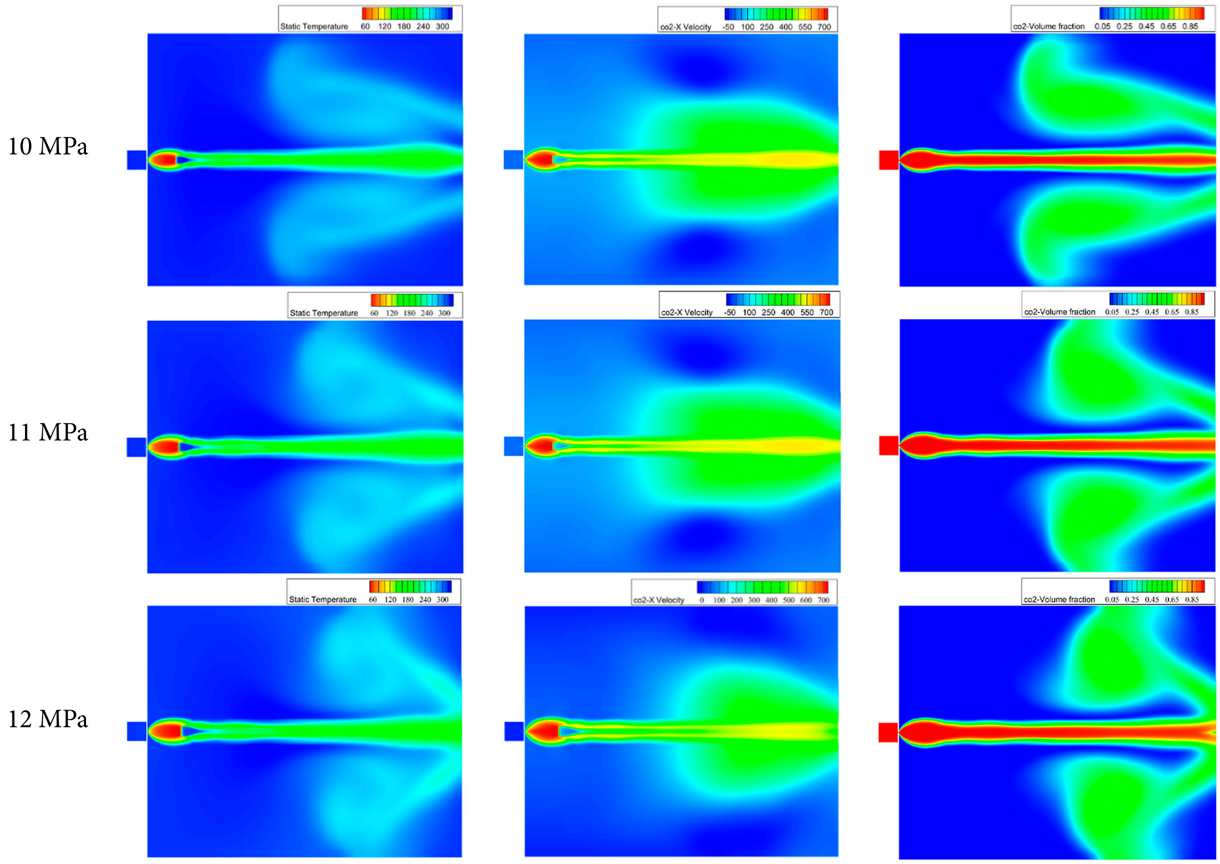

(**a**) Temperature distribution (**b**) Velocity distribution (**c**) Concentration distribution

Figure 6: Cloud diagrams of characteristic parameter distributions after CO_2 leakage under different pipeline transportation pressure conditions.

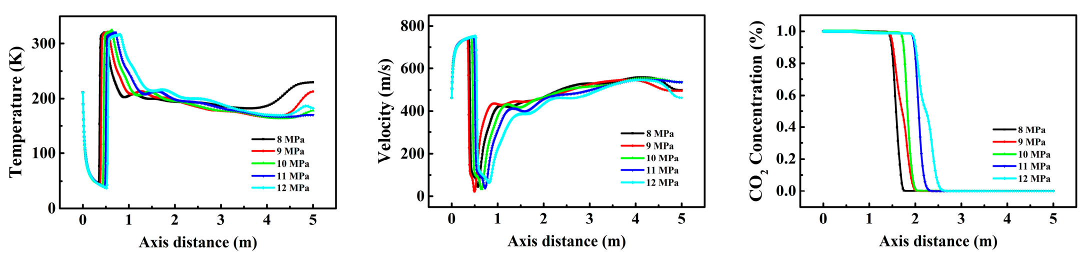

(**a**) Temperature distribution (**b**) Velocity distribution (**c**) Concentration distribution

Figure 7: Distribution curves of axial characteristic parameters after CO_2 leakage under different pipeline transportation pressure conditions.

3.1.3 Pipe Diameter

Fig. 8 shows the cloud diagrams of characteristic parameters after CO_2 leakage under different pipe diameters, and Fig. 9 shows the corresponding axial distributions. Pipe diameter influenced the leakage flow field through the coupled effects of mass flow rate and thermal inertia. In the near-field expansion zone (0–1 m), the 100 mm pipe had a low mass flow rate, weak thermal inertia, and a large relative enthalpy drop. The temperature therefore decreased from the initial 45°C to below 50 K, forming a deep low-temperature core. In contrast, the 500 mm pipe retained more initial internal energy, and the temperature decreased only to about 100 K after expansion. This difference persisted into the far-field warming stage (1–5 m). In the 500 mm case, the larger contact area and higher energy base improved heat exchange, so the temperature exceeded 200 K at 1.5 m. In the 100 mm case, cold retention was stronger, and the temperature remained below 100 K at 2 m before converging to approximately 200 K at 5 m.

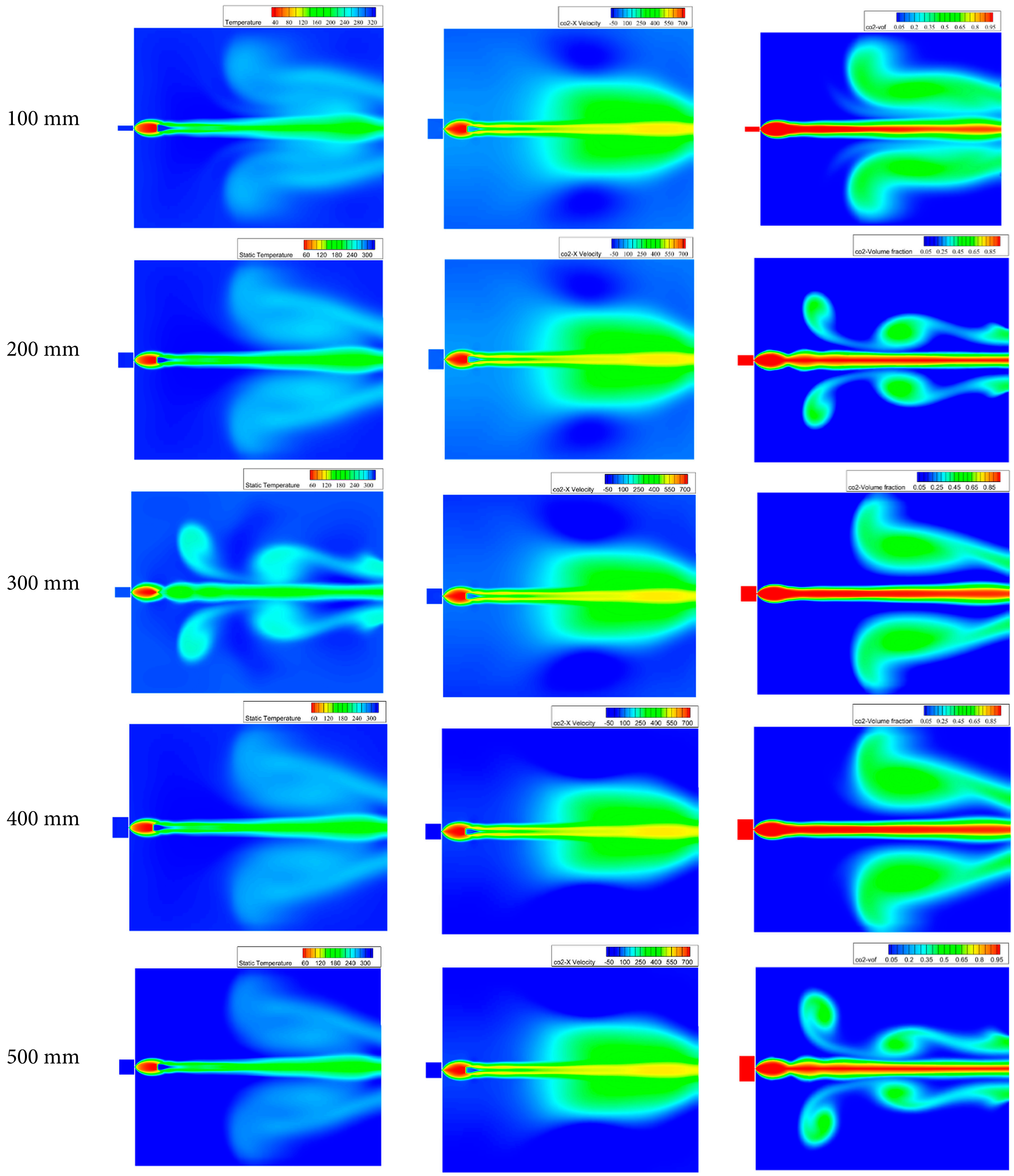

(**a**) Temperature distribution (**b**) Velocity distribution (**c**) Concentration distribution

Figure 8: Cloud diagrams of characteristic parameter distributions after CO_2 leakage under different pipeline diameter conditions.

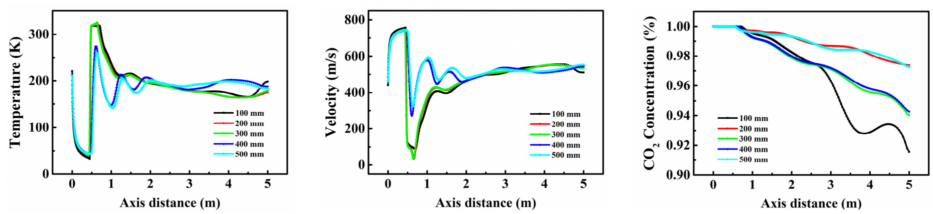

(**a**) Temperature distribution (**b**) Velocity distribution (**c**) Concentration distribution

Figure 9: Distribution curves of axial characteristic parameters after CO_2 leakage under different pipeline diameter conditions.

3.1.4 Leakage Hole Diameter

Fig. 10 shows the cloud diagrams of characteristic parameters after CO_2 leakage under different leak-aperture conditions, and Fig. 11 shows the corresponding axial distributions. Leak aperture controlled the flow field through the coupled effects of mass flow rate and momentum distribution. The 10 mm small-hole case had low mass flow rate and weak thermal inertia, so expansion cooling was strong and the nozzle temperature decreased to below 60 K. Its momentum was concentrated along the jet axis, forming a slender high-velocity (>550 m/s) and high-concentration (>0.85%) core. When the leak aperture increased to 300 mm, representing full pipe-diameter fracture, the much larger mass flow rate produced strong thermal inertia and radial diffusion. The nozzle temperature remained above 220 K, and the jet expanded rapidly in a fan-shaped pattern. The 40 mm large-hole case showed transitional behavior, including lateral widening of the core region and wavy fluctuations of the 0.1–0.3% concentration boundary.

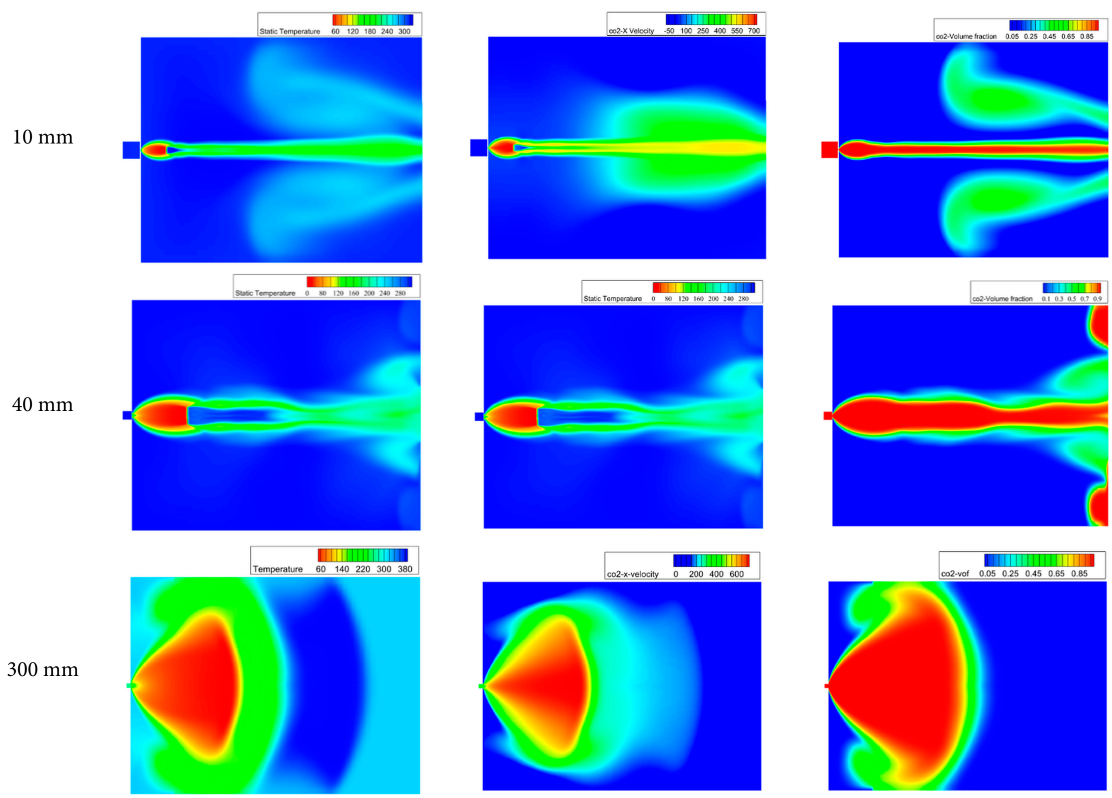

(**a**) Temperature distribution (**b**) Velocity distribution (**c**) Concentration distribution

Figure 10: Cloud diagrams of characteristic parameter distributions after CO_2 leakage under different leakage hole diameter conditions.

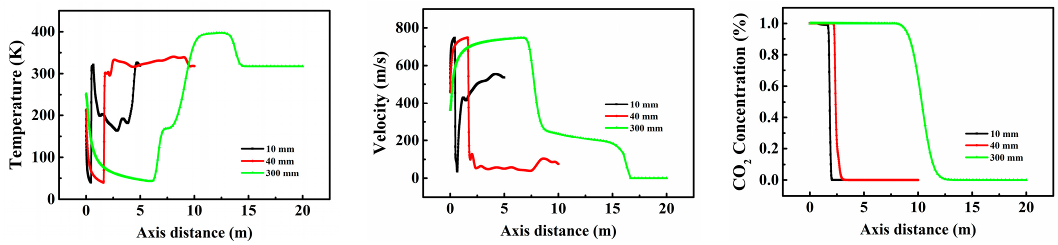

(**a**) Temperature distribution (**b**) Velocity distribution (**c**) Concentration distribution

Figure 11: Distribution curves of axial characteristic parameters after CO_2 leakage under different leakage hole diameter conditions.

3.1.5 Environmental Wind Speed

Fig. 12 shows the cloud diagrams of characteristic parameters after CO_2 leakage under different ambient wind speeds, and Fig. 13 shows the corresponding axial distributions. In these cases, wind direction was defined as a horizontal crosswind perpendicular to the vertically upward leakage jet. Ambient wind speed altered the CO_2 leakage flow field by changing the coupling among turbulent entrainment, momentum exchange, and diffusion dilution. Under the 1 m/s low-wind condition, the jet remained compact and beam-like, and heat exchange with the environment was limited. The deep low-temperature core therefore extended axially, and the temperature at 5 m rose only to approximately 200 K. Under the 5 m/s high-wind condition, stronger ambient entrainment and heat transfer caused the temperature to recover to approximately 250 K at 5 m. The higher wind speed also intensified aerodynamic resistance and turbulent mixing, accelerating momentum dissipation and concentration dilution. At 1 m/s, momentum and mass retention were strong, and the velocity and concentration at 5 m remained approximately 450 m/s and 0.85%, respectively. At 5 m/s, the diffusion range widened slightly, but the core decayed more rapidly, with velocity decreasing to about 350 m/s and concentration falling below 0.75%.

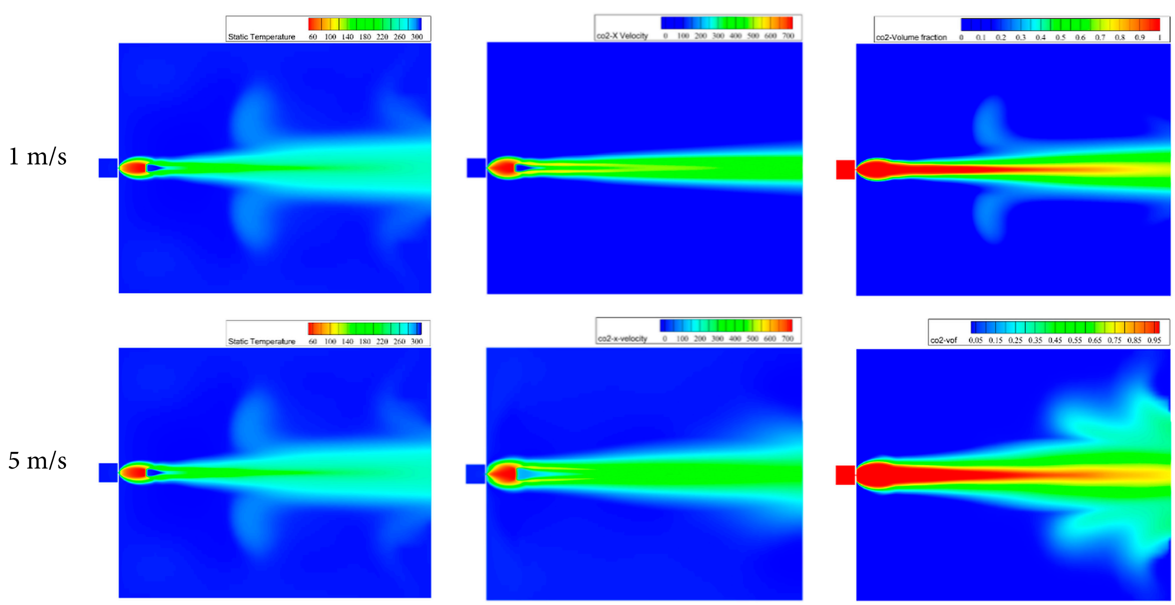

(**a**) Temperature distribution (**b**) Velocity distribution (**c**) Concentration distribution

Figure 12: Cloud diagrams of characteristic parameter distributions after CO_2 leakage under different ambient wind speed conditions.

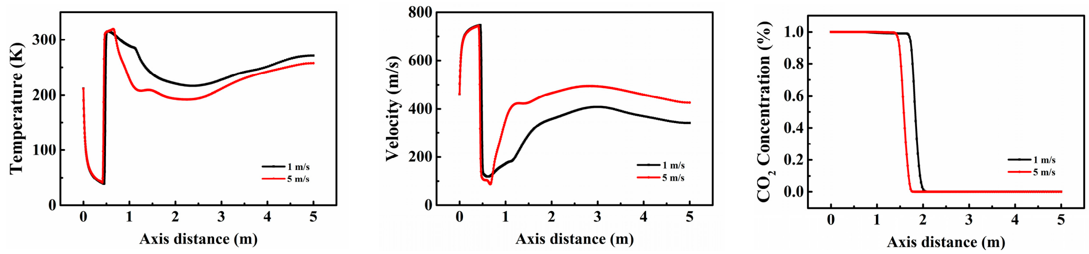

(**a**) Temperature distribution (**b**) Velocity distribution (**c**) Concentration distribution

Figure 13: Distribution curves of axial characteristic parameters after CO_2 leakage under different ambient wind speed conditions.

3.2 Scope of Dry Ice Formation

The dry-ice formation region after CO_2 leakage was controlled by three coupled factors: initial internal energy, expansion-induced enthalpy drop, and environmental heat exchange. Transport temperature and pressure determine the fluid enthalpy and the intensity of Joule-Thomson cooling, and thus provide the internal thermodynamic control on dry ice formation. Pipe diameter and leak diameter regulate mass flow rate and specific surface area, which determine how cold energy accumulates and dissipates. Ambient wind speed changes turbulent entrainment and therefore governs external dilution and warming of the cold plume.

Fig. 14 shows the distribution of dry-ice formation areas under different conditions, and Table 1 summarizes the corresponding mechanisms. Low transport temperature, such as 5°C, reduced the internal energy of the fluid, while high pressure, such as 12 MPa, intensified the expansion enthalpy drop. These two conditions were the primary drivers of large-scale phase change. Leak diameter, pipe diameter, and wind speed mainly regulated the diffusion pattern. Small leak apertures and small pipe diameters favored long, beam-like dry-ice bands because of weak thermal inertia and limited heat exchange. High wind speed enhanced convective heat transfer and weakened cold-energy accumulation, making it the strongest external factor limiting dry-ice extension. Risk assessment should therefore prioritize low-temperature, high-pressure operation and should also consider the hidden risk of small leaks under calm or low-wind conditions.

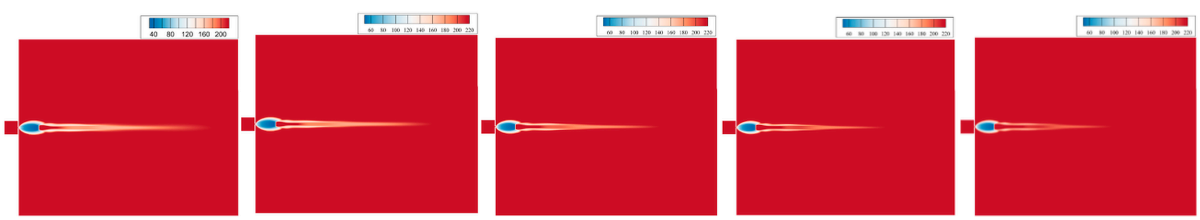

(**a**) Pipeline transportation temperature

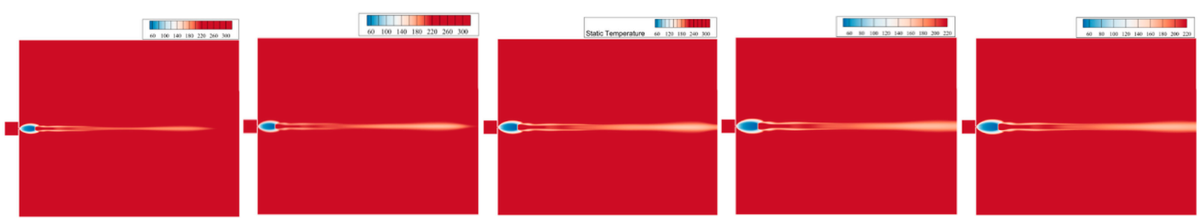

(**b**) Pipeline transportation pressure

Figure 14: *Cont.*

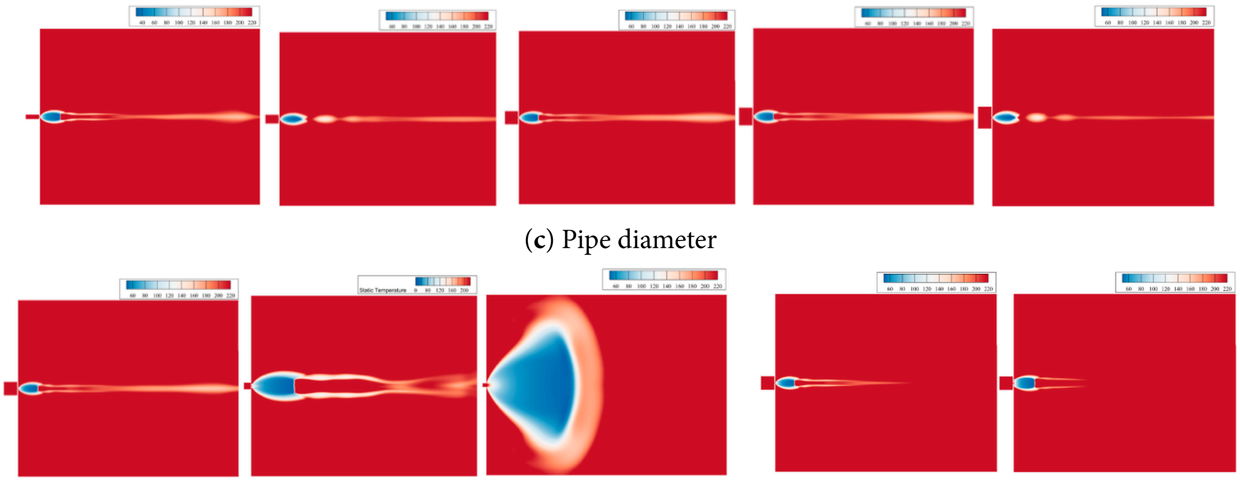

(**c**) Pipe diameter

(**d**) Leakage hole diameter (**e**) Environmental wind speed

Figure 14: Distribution cloud diagrams of solid CO_2 generation areas under different conditions.

Table 1: The influence mechanisms of different factors on the generation range of solid CO_2.

Influencing Factors	**Mechanism**	**Typical Characterization**
Pipeline transport temperature	Low temperature caused the fluid to have a low stagnation enthalpy. After expansion, the remaining energy was insufficient to maintain the gaseous state, and it fell into the solid phase region.	At a temperature of 5°C, the dry ice was distributed the most widely, while at 45°C, it was only generated in a very small area near the nozzle because the coldness was rapidly diluted.
Pipeline transport pressure	The greater the pressure difference was, the more intense the internal energy loss (temperature drop) caused by isentropic expansion was, and the easier it was to pass the CO_2 triple point.	The low-temperature zone was significantly extended under a pressure of 12 MPa, while at a pressure of 8 MPa, dry ice was confined only to the micro-area around the nozzle.
Pipe diameter	The small pipe had a low flow rate and low heat exchange efficiency, which was conducive to maintaining a low core temperature.	At a pipe diameter of 100 mm, the low-temperature zone presented a slender beam, while at a pipe diameter of 500 mm, the low-temperature zone showed dispersed fluctuations, with the range significantly reduced.
Leakage hole diameter	A smaller leakage aperture led to greater internal energy loss and concentrated momentum, while a larger aperture resulted in stronger thermal inertia and a larger contact surface.	Under small aperture, the cooling retention ability was extremely strong, with the dry ice extending the farthest along the axial direction, while under large aperture, it presented a wide fan-shaped distribution.
Environmental wind speed	Strong winds intensified turbulence, drawing in ambient heat and disrupting the cold core of the jet stream.	At a wind speed of 5 m/s, the dry ice zone was significantly shorter than at 1 m/s, and the boundary was unclear, with the heat being rapidly dissipated.

4 Conclusion

(1) This study investigated the effects of transport temperature, pressure, pipe diameter, leak aperture, and ambient wind speed on the CO_2 leakage flow field. Transport temperature controlled the thermodynamic and kinetic basis of jet development. The 45°C case, with higher stagnation enthalpy, delayed the Mach disk to 0.8 m and kept the minimum post-leakage temperature above 100 K. The 5°C case caused the temperature to decrease below 50 K. Pipeline pressure dominated momentum penetration. At 12 MPa, turbulent mixing was strongly suppressed, and CO_2 concentration remained above 0.6% at 2 m from the jet. Pipe diameter and leak aperture modified rewarming through thermal inertia. The 500 mm pipe rewarmed to above 200 K at 1.5 m, whereas the 10 mm leak aperture produced a narrow deep low-temperature core with velocity exceeding 550 m/s. Ambient wind speed promoted CO_2 dilution and plume dispersion. A 5 m/s wind markedly enhanced momentum dissipation and reduced the velocity at 5 m to approximately 350 m/s.

(2) The extent of dry ice formation was governed by initial internal energy, expansion enthalpy drop, and environmental heat exchange. The thermodynamic state was the decisive internal factor because transport temperature and pressure directly determined phase-change intensity. Low temperature (5°C) reduced internal energy, and high pressure (12 MPa) increased the expansion enthalpy drop, producing the widest dry-ice formation range. At 45°C, dry ice was limited to a small region near the nozzle. Geometric boundaries controlled cold accumulation. Small pipe diameters (φ100 mm) and small leak apertures (φ10 mm) produced strong cold retention because of weak thermal inertia and small specific surface area, favoring long axial dry-ice bands. Ambient wind speed was the strongest external factor limiting dry-ice extension. At 5 m/s, enhanced convective heat transfer disrupted the cold jet core, shortened the dry-ice zone, and made its boundary less distinct. These results indicate that low transport temperature, high operating pressure, small leak aperture, and calm-wind conditions should be treated as priority risk conditions for dry-ice prevention and emergency assessment.

Acknowledgement: The authors thank the Technology Inspection Center of Shengli Oilfield, SINOPEC, for providing computational support for this study.

Funding Statement: The authors received no specific funding for this study.

Author Contributions: Hai Yang and Chao Yang contributed to conceptualization, methodology, and original draft preparation. Guoyong Sui and Wendi Yang contributed to software, validation, and data curation. Zongkai Han and Dan Guo contributed to review, editing, and supervision. All authors reviewed and approved the final version of the manuscript.

Availability of Data and Materials: The data supporting the findings of this study are available from the corresponding author upon reasonable request. No new materials were generated in this study.

Ethics Approval: Not applicable. This study does not involve human participants or animal subjects.

Conflicts of Interest: Hai Yang, Chao Yang, Guoyong Sui, Wendi Yang, and Zongkai Han are employees of the Technology Inspection Center of Shengli Oilfield, SINOPEC, which provided computational support for this study as stated in the Acknowledgements. The computational support consisted of access to computing resources. The authors were responsible for the study design, simulations, data interpretation, manuscript preparation, and decision to submit the article. The authors declare no other conflicts of interest.

References

1. Zhang X, Yang X, Lu X. China carbon dioxide capture, utilization and storage annual report. Beijing, China: The Administrative Center for China's Agenda 21; 2023. (In Chinese).
2. Li Y, Zhang J, Fan Z, Li Q, Pan J, Li M, et al. Key technologies for digital intelligence of long-distance CO_2 pipeline and their innovative practices in the Qilu Petrochemical-Shengli Oilfield CO_2 pipeline. Nat Gas Ind. 2024;44(9):1–12. (In Chinese).
3. Haszeldine RS. Carbon capture and storage: how green can black be? Science. 2009;325(5948):1647–52. [CrossRef].
4. IEA. Energy technology perspectives 2020—special report on carbon capture utilization and storage. Paris, France: International Energy Agency; 2020.
5. Global CCS Institute. Global status of CCS 2021. Melbourne, Australia: Global CCS Institute; 2021.
6. Bumb P, Desideri U, Quattrocchi F, Arcioni L. Cost optimized CO_2 pipeline transportation grid: a case study from Italian industries. World Acad Sci Eng Technol. 2009;58:138–45.
7. Mohitrour M, Golshan H, Murray A. Pipeline design & construction: a practical approach. 3rd ed. New York, NY, USA: ASME Press; 2007. [CrossRef].
8. Teng L, Li Y, Zhang D, Ye X, Gu S, Wang C, et al. Evolution and size distribution of solid CO_2 particles in supercritical CO_2 releases. Ind Eng Chem Res. 2018;57(22):7655–63. [CrossRef].
9. Yin B, Huang W, Ouyang X, Zhao X, Meng L, Zhang L, et al. A transient model considering non-equilibrium phase transition in CO_2 pipe decompression. J Pipeline Sci Eng. 2025:100324. [CrossRef].
10. Zhang Z, Lu Z, Yan L, Wang J, Yao S. Experiment and numerical investigation on flow characteristics and near-field structure of dense phase CO_2 pipeline leakage. Process Saf Environ Prot. 2024;182:327–44. [CrossRef].
11. Ibrahim OM, Hansen PM, Bjerketvedt D, Vågsæther K. Evaporation characteristics during decompression of liquified CO_2 from a conical-shaped vessel. Results Eng. 2021;12:100304. [CrossRef].
12. Xing J, Liu Z, Huang P, Feng C, Zhou Y, Zhang D, et al. Experimental and numerical study of the dispersion of carbon dioxide plume. J Hazard Mater. 2013;256:40–8. [CrossRef].
13. Guo X, Yan X, Yu J, Zhang Y, Chen S, Mahgerefteh H, et al. Under-expanded jets and dispersion in supercritical CO_2 releases from a large-scale pipeline. Appl Energy. 2016;183:1279–91. [CrossRef].
14. Guo X, Chen S, Yan X, Zhang X, Yu J, Zhang Y, et al. Flow characteristics and dispersion during the leakage of high pressure CO_2 from an industrial scale pipeline. Int J Greenh Gas Control. 2018;73:70–8. [CrossRef].
15. Teng L, Li Y, Hu Q, Zhang D, Ye X, Gu S, et al. Experimental study of near-field structure and thermo-hydraulics of supercritical CO_2 releases. Energy. 2018;157:806–14. [CrossRef].
16. Jiang X. A review of physical modelling and numerical simulation of long-term geological storage of CO_2. Appl Energy. 2011;88(11):3557–66. [CrossRef].
17. Wang X, Song Z, Pan X, Zhang L, Zhu X, Mei Y, et al. Simulation study on near-field structure and flow characteristics of high-pressure CO_2 released from the pipeline. J Loss Prev Process Ind. 2021;71:104481. [CrossRef].
18. Flechas T, Laboureur DM, Glover CJ. A 2-D CFD model for the decompression of carbon dioxide pipelines using the Peng-Robinson and the Span-Wagner equation of state. Process Saf Environ Prot. 2020;140:299–313. [CrossRef].
19. Pham LHHP, Rusli R. A review of experimental and modelling methods for accidental release behaviour of high-pressurised CO_2 pipelines at atmospheric environment. Process Saf Environ Prot. 2016;104:48–84. [CrossRef].
20. Xiao C, Lu Z, Yan L, Yao S. Transient behaviour of liquid CO_2 decompression: CFD modelling and effects of initial state parameters. Int J Greenh Gas Control. 2020;101:103154. [CrossRef].
21. Liu X, Godbole A, Lu C, Michal G, Venton P. Source strength and dispersion of CO_2 releases from high-pressure pipelines: CFD model using real gas equation of state. Appl Energy. 2014;126:56–68. [CrossRef].
22. Romei A, Persico G. Computational fluid-dynamic modelling of two-phase compressible flows of carbon dioxide in supercritical conditions. Appl Therm Eng. 2021;190:116816. [CrossRef].
23. Witlox HWM, Harper M, Oke A. Modelling of discharge and atmospheric dispersion for carbon dioxide releases. J Loss Prev Process Ind. 2009;22(6):795–802. [CrossRef].
24. Mazzoldi A, Hill T, Colls JJ. Assessing the risk for CO_2 transportation within CCS projects, CFD modelling. Int J Greenh Gas Control. 2011;5(4):816–25. [CrossRef].

25. Woolley RM, Fairweather M, Wareing CJ, Falle SAEG, Proust C, Hebrard J, et al. Experimental measurement and Reynolds-averaged Navier–Stokes modelling of the near-field structure of multi-phase CO_2 jet releases. Int J Greenh Gas Control. 2013;18:139–49. [CrossRef].
26. Woolley RM, Fairweather M, Wareing CJ, Falle SAEG, Mahgerefteh H, Martynov S, et al. CO_2PipeHaz: quantitative hazard assessment for next generation CO_2 pipelines. Energy Procedia. 2014;63:2510–29. [CrossRef].
27. Ahmad M, Lowesmith B, De Koeijer G, Nilsen S, Tonda H, Spinelli C, et al. COSHER joint industry project: large scale pipeline rupture tests to study CO_2 release and dispersion. Int J Greenh Gas Control. 2015;37:340–53. [CrossRef].
28. Bian J, Yu B, Wu S, Chen J, Teng L, Cao X. Near-field vertical diffusion of liquid ammonia leakage. Phys Fluids. 2025;37(3):035133. [CrossRef].
29. Shao Y, Cao X, You W, Zhao S, Nan Z, Bian J. Far-field behavior of supercritical CO_2 being dispersed due to leakage from pipelines. Fluid Dyn Mater Process. 2024;20:2867–85. [CrossRef].
30. Li H, Cao X, Du H, Teng L, Shao Y, Bian J. Numerical simulation of leakage and diffusion distribution of natural gas and hydrogen mixtures in a closed container. Int J Hydrogen Energy. 2022;47(84):35928–39. [CrossRef].
31. Bian J, Yu B, Cao H, Bai H, Cao X, Guo D. Carbon dioxide condensation: theory, phenomenon and application. Chem Eng J Adv. 2025;24:100954. [CrossRef].
32. Menter FR. Two-equation eddy-viscosity turbulence models for engineering applications. AIAA J. 1994;32(8):1598–605. [CrossRef].
33. Shih TH, Liou WW, Shabbir A, Yang Z, Zhu J. A new k-ϵ eddy viscosity model for high Reynolds number turbulent flows. Comput Fluids. 1995;24(3):227–38. [CrossRef].